Fabrication of Cu_6Sn_5 Intermetallic Nanoarrays on Cu Wires and Electrochemical Detection of Uric Acids

Haoran SUI, Jin QIAN, Hao HUANG, Zhenhua DAN *

College of Materials Science and Engineering, Nanjing Tech University, Nanjing 211816, China

http://doi.org/10.5755/j02.ms.42393

Received 30 July 2025; accepted 11 September 2025

Stepwise process, including surface alloying in molten tin and chemical dealloying, has been employed to fabricate Cu_6Sn_5 intermetallic arrays sensors to uric acid. The Cu_6Sn_5 intermetallics (IMCs) form through the interdiffusion of Sn into Cu in the liquid-solid reaction at 300 ºC during immersion of Cu wire in molten Sn, which triggers the bottom-to-up growth of ordered alignments and better interface strength. The Cu_6Sn_5 IMC arrays are leached out through the selective dissolution of embedded Sn in the voids and Sn shell during the chemical dealloying. The formation of the Cu_6Sn_5 IMC arrays is governed by the micro-coupling effects. On the basis of differential pulse voltammetry (DPV) measurements, the Cu_6Sn_5 IMC arrays, as an electrochemical sensor, possess a sensitivity of 0.0184 μA μM, which is 16 times higher than the original Cu wires. The enhanced sensitivity is attributed to the increased surface area and improved oxidation kinetics of Cu_6Sn_5 IMC nanoarrays.

Keywords: surface alloying, chemical dealloying, Cu_6Sn_5 intermetallics, differential pulse voltammetry, uric acid.

1. INTRODUCTION

Uric acid ($C_5H_4N_4O_3$, UA) has been implicated as a risk factor and cause of numerous disease states. A range of serum UA concentrations has been defined for both hyperuricemia and hypouricemia. Hyperuricemia has been defined for men as a UA concentration greater than 420 μM [1, 2]. For women, most studies define hyperuricemia as a concentration greater than approximately 360 μM [1, 2]. Hypouricemia is generally defined as a UA concentration of less than approximately 120 μM [3]. Thus, the normal range of UA concentration falls somewhere between 120 and 380 μM, varying slightly depending on gender. Since the basal concentration of UA and ascorbic acid in physiological samples varies depending on the matrix across a wide range from 1.0×10^{-7} to 1.0×10^{-3} mol L^{-1} [4], both sensitivity and selectivity are of equal importance in developing an electrochemical assay. An abnormally high UA level has been correlated with gout, hypertension, cardiovascular disease, and renal disease, whereas a reduced UA concentration has been linked to multiple sclerosis, Parkinson's disease, Alzheimer's disease, and optic neuritis. Historically, UA has been considered a marker of these disease states. Accurate detection and analysis of UA and creatinine levels in human blood and urine are of importance for the monitoring of the specific diseases.

Many methods, including fluorescence spectroscopy [5], high-performance liquid chromatography [6], capillary zone electrophoresis [7], and liquid chromatography-tandem mass spectrometry [8], have been utilized for the detection of UA. Although these methods have high accuracy and sensitivity, they still suffer from the requirements of expensive instruments and complex operation protocols. In the past decades, electrochemical techniques have been considered as reliable and promising replacements because of their specificity, high sensitivity, rapidity, ease of miniaturization, simple operation, and low price [9]. Particularly, amperometry and differential pulse voltammetry techniques are extremely sensitive and selective for the detection of easily oxidizable UA. Therefore, the electrochemical method is best for the determination of electroactive compounds DA and UA.

Many kinds of nano-sized electrochemical sensors, composed of noble metals, have been developed recently for fast detection of UA, such as reduced graphene oxide nanomaterials anchored with Pd–Pt bimetallic nanoparticles [10], CdTe nanoparticles [11], nanoporous Au [12, 13], hierarchical nanoporous PtCu alloy on a glassy carbon electrode for UA in the concentration ranges from 10 to 70 μM [14]. Doped $ZnO/Ag_2O/Co_3O_4$ nanoparticles on a glassy carbon electrode exhibit a good detection range of 0.1 nM – 0.01 mM and a high sensitivity of 82.3323 μA μM^{-1} cm^{-2} [15]. Cu-based UA electrochemical sensors possess the cost-effectiveness and good performance [16, 17]. Mercaptosuccinic acid-modified Cu nanoparticles exhibit a the linear range of UA was 5 μM – 4.5 mM with a limit of detection of 3.7 μM [18]. The nanomization of the Cu-based sensors can effectively improve the sensitivity to UA. The dealloying is helpful to generate the nanoporosity with a few tenth nanometers. Recently, the chemical dealloying has been employed to fabricate the Cu_6Sn_5 IMC nanoarrays to increase the surface area [19]. Dealloying, a common method for preparing many porous metals, involves selectively dissolving a specific alloy component in acidic or alkaline solutions to create a porous structure [20]. The nanoporous structure is impossible to form on pure metallic precursors due to the absence of the key difference in the electrochemical instability between the phases or alloying elements in pure metals or their foam-

* Corresponding author: Z. Dan
E-mail: *zhenhuadan@njtech.edu.cn*

type counterparts [21]. A stepwise fabrication method has been developed for intermetallic arrays on Cu foams [19]. The Cu_6Sn_5 IMC nanoarrays are expected to have better UA detection performance than the Cu wires through the surface roughening and dealloying.

The diffusion behavior of Cu in molten Sn, coupled with their contrasting reactivity in acidic medias [22], suggests that the pairing of Cu and Sn offers a promising strategy for creating the proper dealloying precursors with layered intermetallic distributions and relatively high difference in the electrochemical activity. A stepwise process, including first surface alloying in molten Sn and sequential chemical dealloying, is employed to roughen Cu wires. The nano-sized Cu_6Sn_5 IMC nanoarrays are anticipated to form through the selective dissolution of embedded Sn in the form of micro-couplings, and further improve the oxidation of UA on the surface.

2. EXPERIMENTAL PROCEDURE

The commercial Cu wires (purity: 99.95 wt.%) with a diameter of 1 mm were supplied by Guangzhou Lige Technology Co., Ltd. Sn particles (purity: 99.5 wt.%) were purchased from Beijing Zhongcheng New Materials Co., Ltd. All other reagents, including concentrated hydrochloric acid (HCl), Uric acid (UA), and anhydrous ethanol, were of analytical grade. The fabrication procedures of stepwise fabrication of Cu_6Sn_5 intermetallic arrays are shown in Fig. 1. In Step I, Cu wires were alloyed with molten Sn (99.99 wt.%) at 300 °C for 10 min to form the Sn-alloyed layers. In Step II, chemical dealloying of Sn-alloyed Cu wires was conducted in 0.1 M HCl for 48 h.

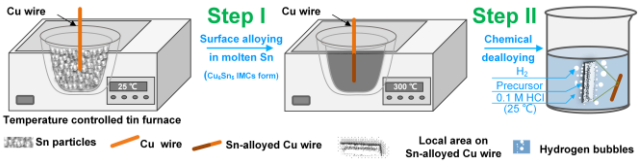

Fig. 1. Schematics of stepwise fabrication of Cu_6Sn_5 intermetallic arrays after surface alloying in molten Sn and chemical dealloying in 0.1 M HCl solution

Before observing the morphology, the Sn-alloyed and dealloyed samples were embedded in the resin, then polished and pickled in a micro-etching solution composed of 2 g $FeCl_3$, 5 ml HCl, 30 ml H_2O and 60 ml ethanol for 40 s according to ASTM E407-99. The morphology of dealloyed Sn-alloyed Cu wires was characterized by scanning electron microscopy (SEM, FEI Talos, F200X). Electrochemical measurements were carried out using a CHI760E electrochemical workstation (Shanghai Chenhua Instrument Co., Ltd.).

All the three-electrode electrochemical measurements were set as using Cu wires and the Cu_6Sn_5 intermetallic arrays electrode as the working electrode, the Pt electrode as the counter electrode, and Ag/AgCl as the reference electrode. The performance of the as-fabricated electrode as a sensor was measured in 0.1 M phosphate buffer solution (PBS) at pH 7.0 by using differential pulse voltammetry (DPV) with an UA concentration of 10 μM to 500 μM. The range of the potential was set between -0.5 V and 0.5 V, and the scan rate was 100 mV s^{-1}. The cyclic voltammetry was used to judge the reaction characteristics at the various scanning rates of 25 – 100 mV s^{-1} in PBS solution. The temperature was set at 37 °C. The 3-5 parallel samples were tested under the same conditions.

3. RESULTS AND DISCUSSION

3.1. Formation of Cu_6Sn_5 intermetallic nano-arrays after surface alloying in molten Sn and chemical dealloying

As shown in Fig. 2 a, a layered structure formed outside of Cu core after immersing Cu wire into molten Sn for 10 min. As shown in Fig. 2 b, two layer,s including Sn shell and an interconnected rod-like occupied layer with a thickness of approximately 50 μm were formed through the liquid-solid interfacial reactions between molten Sn and solid Cu. A light contrast of an outmost layer indicates that Sn with a large molecular weight is enriched. A gray contrast in an interlayer suggests that Cu elements are distributed. The structure in Fig. 2 c, similar with porous metals, can be observed the void formation after micro-etching. This fact proves the possibility of the primary dissolution of Sn. The morphology in Fig. 2 d and the mapping profiles of Cu in Fig. 2 e reflected the difference in Cu concentration in the interlayer. The Cu_6Sn_5 phase and Sn are primarily formed from the eutectic reaction at 227 °C [23]. The line scan data of Cu and Sn elements in Fig. 2 f demonstrates the formation of Cu_6Sn_5 IMCs based on the elemental ratio of Cu/Sn. It is worth noting that β-Sn phases are certainly distributed in the voids of Cu_6Sn_5 IMCs.

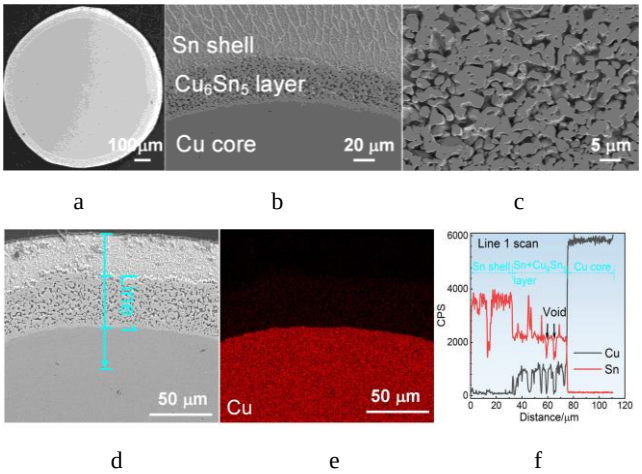

Fig. 2. a – cross-sectional morphology of Cu wire; b – low-magnified; c – high-magnified of layered structure on Cu wire including Sn shell, Cu_6Sn_5 intermetallic layer and Cu core. d – corresponding SEM morphology; e – Cu distribution profile; f – distribution profiles of Cu and Sn elements along Line 1 in d of Sn-alloyed Cu wire after micro-etching according to ASTM E407-99

When Sn-alloyed Cu wires were immersed in 0.1 M HCl solution for 48 h, the outermost Sn shell was completely dissolved out as shown in the cross-sectional morphology in Fig. 3 a and b. The high-magnification SEM morphology in Fig. 3 c shows a similar morphology to that in Fig. 2 c. Due to the invasion of resin into the voids where Sn phases are distributed in the interlayer of Cu, these dark-

gray contrast regions represent resin in Fig. 3 c. The elemental mappings of Sn in Fig. 3 d and Cu in Fig. 3 e demonstrate that Cu and Sn are distributed at the same position. Meanwhile, the same fluctuation of the Cu and Sn concentration along Line 2 in Fig. 3 f proves the presence of Cu_6Sn_5 IMCs.

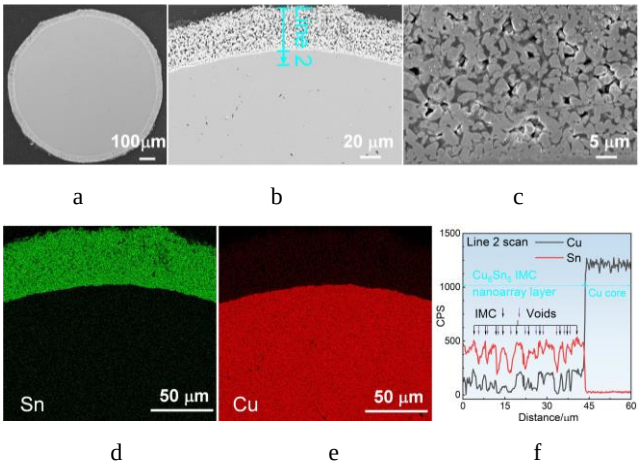

Fig. 3. a – cross-sectional morphology of Cu wire; b – low-magnification; c – high-magnification of dealloyed Sn-alloyed Cu wire including Cu_6Sn_5 intermetallic nanoarrays layer and Cu core; d – corresponding mapping profile of Sn; e – profile of Cu; f – distribution profiles of Cu and Sn elements along Line 2 in b of dealloyed Sn-alloyed Cu wire after micro-etching according to ASTM E407-99

On the basis of the similarity between the morphology in Fig. 2 and Fig. 3, the voids arose from the primary dissolution of the embedded Sn phase in the interlayer, and Cu_6Sn_5 IMCs were distributed as previously formed in Sn-alloyed Cu wires. The up-ward aligned Cu_6Sn_5 nanorods uniformly spread on the surface of Cu wires as shown in top-view SEM morphology (Fig. 4 a – c). The concentration-driven interdiffusion of Sn atoms into Cu matrix and the large difference in the diffusivity between the liquid-solid reactions and solid-solid reactions motivate the two-dimensional growth of Cu_6Sn_5 IMCs. The mean diameter of rod-shaped Cu_6Sn_5 IMCs was measured to be 88.5 nm. The mean length was 281.8 nm, and the length changed from a few-tenth nanometers to a few micrometers. The ratio of the length-to-diameter was approximately 3.2. The present structure is defined as Cu_6Sn_5 IMC nanoarrays.

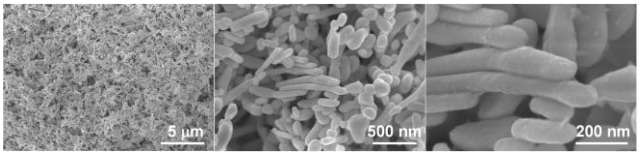

Fig. 4. Top-view SEM morphology of Sn-alloyed Cu wire after dealloying in 0.1 M HCl solution for 48 h with magnification: a – 77; b – 500; c – 2000

The electrochemical stability of the involved phases is compared in Fig. 5. The corrosion potentials for pure Sn and Cu in 0.1 M HCl solution are measured at -0.48 V and -0.08 V, respectively, while Cu_6Sn_5 IMCs exhibit a corrosion potential of -0.47 V. The potential difference between Cu/Sn and Sn/Cu_6Sn_5 couplings was approximately 470 mV and 10 mV, respectively. During chemical dealloying of Sn-alloyed Cu wires, the anodic dissolution of the embedded Sn within the voids of Cu_6Sn_5 IMC nanoarrays is initiated and driven by the micro-galvanic coupling effect, as evidenced by the evolution of phase composition and morphology (Fig. 2 – Fig. 4).

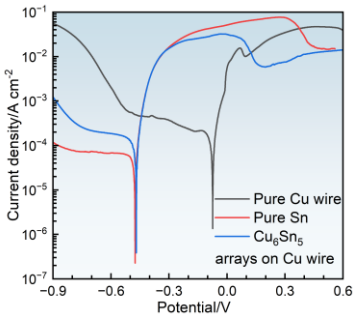

Fig. 5. Potentiodynamic polarization curves of pure Cu wires, pure Sn plates and dealloyed Sn-alloyed Cu wires in 0.1 M HCl solution. Scan rate: 1 mV s^{-1}

The micro-coupling effects are considered as the main mechanism for the formation of Cu_6Sn_5 IMCs nanoarrays. The present nanoarrays are expected to have a superior detection performance for UA.

3.2. Evaluation of the detection sensitivity of uric acids by Cu_6Sn_5 intermetallic nanoarrays electrochemical sensors

The detection performance of Cu_6Sn_5 IMC nanoarrays electrochemical sensors (abbreviated as CNS) was evaluated by using DPV and CV methods, and the collected curves are shown in Fig. 6. There is an oxidation peak centered at -0.09 V. The peak current can be regarded as a rule to judge the oxidation of UA. The well consistency of peak potential in Fig. 6 a demonstrated that the present CNSs have a good electrochemical stability. When UA is dissolved into PBS solution, the peak current corresponding to the oxidation of UA is observed by CNSs with the UA dosages. A good linearity between the peak currents and UA concentrations is obtained with a coefficient of determination of 0.97. The sensitivity of CNSs is calculated to be 0.0184 μA μM. On the other hand, when the Cu wires are used as electrochemical sensors, the peak currents change from 0.90 μA to 1.66 μA. The sensitivity of Cu wires is calculated to be 0.00116 μA μM. The CNSs possess about 16 times higher sensitivity than Cu wires. As shown in Fig. 6 b, the peak current at the potential of about 0.1 V changes from 0.25 mA to 0.76 mA with increase of scan rates from 25 to 100 mV s^{-1}. The inset of the linear fitting of peak current density vs square root of scan rates in Fig. 6 b demonstrates that the oxidation kinetics is diffusion controlled.

The oxidation of UA at pH higher than 6 udergoes a two-electron oxidation reaction accompanied with quinoid formation and final decomposition for allantion [24]. When the electrochemical sensor electrodes have been modified by Au nanoparticles [25] and functionalized multiwall carbon nanotubes combined with Nafion and both Au and Pt nanoparticles [26], the better conductivity enhances the

reactivity and improves the passing of the electrons from the half-cell reactions. The present Cu-based CNSs have better cost-effectiveness than noble metal based sensors mentioned [10, 12, 13, 24 – 26]. On the other hand, the introduction of uniform and tailored mesoporous carbons drastically increases specific surface area and activity [27]. As shown in Fig. 4, the average diameter of Cu_6Sn_5 IMCs is 88.5 nm, and the Cu cores is wholly covered by CNSs. The high specific surface area is certainly provided by the nano-sized CNSs. Moreover, the adherent Cu_6Sn_5 IMCs presented here anchor on the Cu wires due to the thermal alloys in molten Sn and the bottom-to-up growth of Cu_6Sn_5 IMCs in Fig. 1, Fig. 3, and Fig. 4. The good conductivity is accessed by the metallic chemical composition of Cu and Sn in CNSs (Fig. 3, Fig. 4). The unique nanostructure of CNSs is able to maintain the structural integration during the long-term service compared with nanoparticle-type [10, 18, 25] and coating-type [15, 26] sensors. As has been reported before, a three-dimensional porous Cu_6Sn_5 anode for Li`s batteries via electroless plated Sn on Cu foams shows superior electrochemical performance and a rechargeable capacity of 404 mA h g^{-1} over 100 cycles [28]. This is attributed to high surface area, improved interface strength, and structural stability [28 – 30]. In fact, Sn alloying into Cu effectively depresses the volume expansion during the oxidation reactions and promotes the activity of oxidation reactions [31 – 33]. The high surface area and good conductivity of CNSs synergetically improve the electrochemical sensing performance.

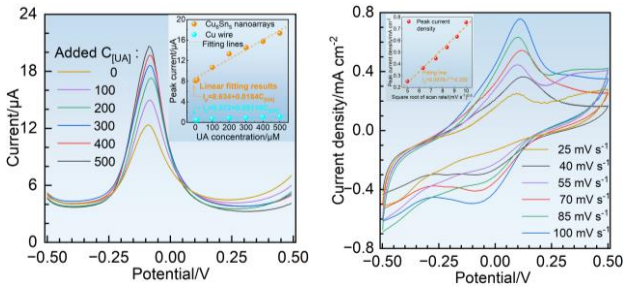

a b

Fig. 6. a – DPV curves of dealloyed Sn-alloyed Cu wires in PBS solution with different UA concentrations with scan rate of 100 mV s^{-1}; b – CV curves of dealloyed Sn-alloyed Cu wires in PBS solution with different scan rates of 25 – 100 mV s^{-1}

4. CONCLUSSIONS

A stepwise process, including surface alloying in molten tin and chemical dealloying, was used to fabricate Cu_6Sn_5 intermetallic nanoarrays. An interdiffusion of Sn into Cu during the liquid-solid reaction at 300 ºC after immersion of Cu wire in molten Sn for 10 min promoted the formation of upward-aligned Cu_6Sn_5 IMCs. The bottom-to-up growth of Cu_6Sn_5 IMCs during immersion in molten Sn helps to improve the ordered alignments and interface strength. Chemical dealloying, governed by the micro-coupling effects, leached out the Sn shell and embedded Sn in the voids and resulted in the formation of the Cu_6Sn_5 IMC arrays. Differential pulse voltammetry (DPV) and cyclic voltammetry (CV) measurements reveal that the Cu_6Sn_5 IMC nanoarrays with an average diameter of 88.5 nm, as an electrochemical sensor, possess a sensitivity of 0.0184 μA μM, 16 times higher than the original Cu wires. The enhanced sensitivity is attributed to the increased surface area and improved oxidation kinetics of Cu_6Sn_5 IMC nanoarrays. This stepwise fabrication method is good at void control and formation of anchored arrays of Sn-based intermetallics by changing the time duration, and the temperature of molten Sn.

Acknowledgments

This work is financially supported by the National Science and Technology Major Project of the Ministry of Science and Technology of China, the National Key Research and Development Program of China (No. 2022YFB3705500) and the National Natural Science Foundation of China under (Grant no. 52371157). This work is partially supported by Priority Academic Program Development of Jiangsu Higher Education Institution (PAPD) and Top-Notch Academic Programs Project of Jiangsu Higher Education Institutions-TAPP (No. PPZY2015B128).

REFERENCES

1. **Waring, W.S., Webb, D.J., Maxwell, S.R.J.** Uric Acid as A Risk Factor for Cardiovascular Disease *QJM: An International Journal of Medicine* 93 (11) 2000: pp. 707 – 713. https://doi.org/10.1093/qjmed/93.11.707
2. **Johnson, R.J., Kang, D.H., Feig, D., Kivlighn, S., Kanellis, J., Watanabe, S., Tuttle, K.R., Rodriguez-Iturbe, B., Herrera-Acosta, J., Mazzali, M.** Is There a Pathogenetic Role for Uric Acid in Hypertension and Cardiovascular and Renal Disease *Hypertension* 41 (6) 2003: pp. 1183 – 1190. https://doi.org/10.1161/01.HYP.0000069700.62727.C5
3. **Hisatome, I., Tsuboi, M., Shigemasa, C.** Renal Hypouricemia *Nihon Rinsho. Japanese Journal of Clinical Medicine* 54 (12) 1996: pp. 3337 – 3342. PMID: 8976116.
4. **Capella, P., Ghasemzadeh, B., Mitchell, K., Adams, R.N.** Nafion-coated Carbon-fiber Electrodes for Neurochemical Studies in Brain Tissue *Electroanalysis* 2 (3) 1990: pp. 175 – 182. https://doi.org/10.1002/elan.1140020303
5. **Galbán, J., Andreu, Y., Almenara, M.J., Marcos, S.D., Castillo, J.R.** Direct Determination of Uric Acid in Serum by A Fluorometric-enzymatic Method Based on Uricase *Talanta* 54 (5) 2001: pp. 847 – 854. https://doi.org/10.1016/S0039-9140(01)00335-6
6. **Zuo, Y.G., Wang, C.J., Zhou, J.P., Sachdeva, A., Ruelos, V.C.** Simultaneous Determination of Creatinine and Uric Acid in Human Urine by High-performance Liquid Chromatography *Analytical Sciences* 24 (12) 2008: pp. 1589 – 1592. https://doi.org/10.2116/analsci.24.1589
7. **Xing, X.P., Shi, X., Zhang, M.J., Jin, W., Ye, J.N.** CE Determination of Creatinine and Uric Acid in Saliva and Urine during Exercise *Chromatographia* 67 (11) 2008: pp. 985 – 988. https://doi.org/10.1365/s10337-008-0599-1
8. **Ma, Q.S., Wang, Q., Zhao, K.S., Zhai, S.B., Liu, S., Liu, Z.Q.** UPLC-MS/MS Method for Determination of Uric Acid and Creatinine in Serum and Urine of Hyperuricemic

Mice *Chemical Journal of Chinese University-Chinese* 34 (12) 2013: pp. 2716 – 2720. https://doi.org/10.7503/cjcu20130704

9. **Income, K., Ratnarathorn, N., Khamchaiyo, N., Srisuvo, C., Ruckthong, L., Dungchai, W.** Disposable Nonenzymatic Uric Acid and Creatinine Sensors Using μPAD Coupled with Screen-printed Reduced Graphene Oxide-gold Nanocomposites *International Journal of Analytical Chemistry* 2019 (1) 2019: pp. 3457247. https://doi.org/10.1155/2019/3457247
10. **Yan, J., Liu, S., Zhang, Z.Q., He, G.W., Zhou, P., Liang, H.Y., Tian, L.L., Zhou, X.M., Jiang, H.J.** Simultaneous Electrochemical Detection of Ascorbic Acid, Dopamine and Uric Acid Based on Graphene Anchored with Pd–Pt Nanoparticles *Colloids and Surfaces B: Biointerfaces* 111 2013: pp. 392 – 397. http://dx.doi.org/10.1016/j.colsurfb.2013.06.030
11. **Jin, D., Seo, M.H., Huy, B.T., Pham, Q.T., Conte, M.L., Thangadurai, D., Lee, Y.I.** Quantitative Determination of Uric Acid Using CdTe Nanoparticles as Fluorescence Probes *Biosensors and Bioelectronics* 77 2016: pp. 359 – 365. https://doi.org/10.1016/j.bios.2015.09.057
12. **Shang, K.S., Wang, S.J., Chen, S.Y., Wang, X.** Sensitivity Detection of Uric Acid and Creatinine in Human Urine Based on Nanoporous Gold *Biosensors* 12 2022: pp. 588. https:// doi.org/10.3390/bios12080588
13. **Shi, Y.T., Wang, J., Li, S.M., Yan, B., Xu, H., Zhang, K., Du, Y.K.** The Enhanced Photo-electrochemical Detection of Uric Acid on Au Nanoparticles Modified Glassy Carbon Electrode *Nanoscale Research Letters* 12 (1) 2017: pp. 455. https:// doi.org/10.1186/s11671-017-2225-3
14. **Zhao, D.Y., Fan, D.W., Wang, J.P., Xu, C.X.** Hierarchical Nanoporous Platinum-copper Alloy for Simultaneous Electro-chemical Determination of Ascorbic Acid, Dopamine, and Uric Acid *Microchimica Acta* 182 (7) 2015: pp. 1345 – 1352. https://doi.org/10.1007/s00604-015-1450-7
15. **Alam, M.M., Asiri, A.M., Uddin, M.T., Islam, M.A., Awual, M.R., Rahman, M.M.** Detection of Uric Acid Based on Doped ZnO/Ag_2O/Co_3O_4 Nanoparticle Loaded Glassy Carbon Electrode *New Journal of Chemistry* 43 (22) 2019: pp. 8651 – 8659. https://doi.org/10.1039/c9nj01287g
16. **Selvaraju, T., Ramaraj, R.** Simultaneous Detection of Ascorbic Acid, Uric Acid and Homovanillic Acid at Copper Modified Electrode *Electrochimica Acta* 52 2007: pp. 2998 – 3005. https://doi.org/10.1016/j.electacta.2006.09.032
17. **Krishnamoorthy, K., Sudha, V., Kumar, S.M.S., Thangamuthu, R.** Simultaneous Determination of Dopamine and Uric Acid Using Copper Oxide Nano-rice Modified Electrode *Journal of Alloys and Compounds* 748 2018: pp. 338 – 347. https://doi.org/10.1016/j.jallcom.2018.03.118
18. **Ma, C.Y., Kong, L.B., Sun, X.Y., Zhang, Y.C., Wang, X.Y., Wei, X.W., Wan, H., Wang, P.** Enzyme-free and Wide-range Portable Colorimetric Sensing System for Uric Acid and Hydrogen Peroxide Based on Copper Nanoparticles *Talanta* 255 2023: pp. 124196. https://doi.org/10.1016/j.talanta.2022.124196
19. **Tao, C.Y., Tu, M.S., Huang, H., Chang, H., Dan, Z.H.** Tri-modal Hierarchical Nanoporous Copper as Hydrogen Evolution Reaction Catalysts with Low Tafel Slopes via Stepwise Fabrication of Surface Alloying in Molten Tin and Electrochemical Dealloying of Copper Foams *Journal of Alloys and Compounds* 1037 2025: pp. 182391. https://doi.org/10.1016/j.jallcom.2025.182391
20. **McCue, I., Benn, E., Gaskey, B., Erlebacher, J.** Dealloying and Dealloyed Materials *Annual Review of Materials Research* 46 (1) 2016: pp. 263 – 286. https://doi.org/10.1146/annurev-matsci-070115-031739
21. **Li, J., Hu, S.Y., Li, Y.L., Shi, S.Q.** Evolution Mechanisms and Kinetics of Porous Structures during Chemical Dealloying of Binary Alloys *Microporous and Mesoporous Materials* 320 2021: pp. 111092. https://doi.org/10.1016/j.micromeso.2021.111092
22. **Banerjee, A., Kumar, R., Dutta, M., Bysakh, S., Bhowmick, A.K., Laha, T.** Microstructural Evolution in Cu-Sn Coatings Deposited on Steel Substrate and Its Effect on Interfacial Adhesion *Surface and Coating Techonology* 262 2015: pp. 200 – 209. https://doi.org/10.1016/j.surfcoat.2014.12.049
23. **Wang, J.T., Lv, Z.W., Zhang, L.B., Duan, F.C., Wang, J.Q., Li, F.Q., Chen, H.T., Li, M.Y.** Nucleation and Growth of Cu_6Sn_5 during The Aging Process of Cu/Sn Interface in Electronic Packaging-by In-situ TEM *Acta Materialia* 264 2024: pp. 119581. https://doi.org/10.1016/j.actamat.2023.119581
24. **Lakshmi, D., Whitcombe, M.J., Davis, F., Sharma, P.S., Prasad, B.B.** Electrochemical Detection of Uric Acid in Mixed and Clinical Samples: A Review *Electroanalysis* 23 2011: pp. 305 – 320. https://doi.org/10.1002/elan.201000525
25. **Stoeva, S.I., Lee, J.S., Thaxton, C.S., Mirkin, C.A.** Multiplexed DNA Detection with Biobarcoded Nanoparticle Probes *Angewandte Chemie International Edition* 45 2006: pp. 3303 – 3306. https://doi.org/10.1002/anie.200600124
26. **Antoine, O., Bultel, Y., Durand, R.** Oxygen Reduction Reaction Kinetics and Mechanism on Platinum Nanoparticles inside Nafion® *Journal of Electroanalytical Chemistry* 499 (1) 2001: pp. 85 – 94. https://doi.org/10.1016/S0022-0728(00)00492-7
27. **Jun, S., Joo, S.H., Ryoo, R., Kruk, M., Jaroniec, M., Liu, Z., Ohsuna, T., Terasaki, O.** Synthesis of New, Nanoporous Carbon with Hexagonally Ordered Mesostructure *Journal of the American Chemical Society* 122 (43) 2000: pp. 10712 – 10713. https://doi.org/10.1021/ja002261e
28. **Xue, L.G., Fu, Z.H., Yao, Y., Huang, T., Yu, A.S.** Three-dimensional Porous Sn–Cu Aloy Anode or Lithium-ion Batteries *Electrochimica Acta* 55 (24) 2010: pp. 7310 – 7314. https://doi.org/10.1016/j.electacta.2010.07.015
29. **Yang, C.G., Zhang, D.W., Zhao, Y.B., Lu, Y.H., Wang, L., Goodenough, J.B.** Nickel Foam Supported Sn–Co Alloy Film as Anode for Lithium Ion Batteries *Journal of Power Sources* 196 (24) 2011: pp. 10673 – 10678. https://doi.org/10.1016/j.jpowsour.2011.08.089
30. **Yang, T.L., Aoki, T., Matsumoto, K., Toriyama, K., Horibe, A., Mori, H., Orii, Y., Wu, J.Y., Kao, C.R.** Full Intermetallic Joints for Chip Stacking by Using Thermal Gradient Bonding *Acta Materialia* 113 2016: pp. 90 – 97. https://doi.org/10.1016/j.actamat.2016.04.046
31. **Su, L., Fu, J., Zhang, P., Wang, L., Wang, Y., Ren, M.** Uniform Core–shell Cu_6Sn_5@C Nanospheres with Controllable Synthesis and Excellent Lithium Storage Performances *RSC Advances* 7 (45) 2017: pp. 28399 – 28406.

https://doi.org/10.1039/c7ra02214j

32. **Ying, H., Han, W.Q.** Metallic Sn-based Anode Materials: Application in High-performance Lithium-ion and Sodium-ion Batteries *Advanced Science* 4 (11) 2017: pp. 1700298. https://doi.org/10.1002/advs.201700298

33. **Chen, J., Yang, L., Fang, S., Zhang, Z., Hirano, S.I.,** Facile Fabrication of Graphene/Cu_6Sn_5 Nanocomposite as The High Performance Anode Material for Lithium Ion Batteries *Electrochimica Acta* 105 2013: pp. 629 – 634. https://doi.org/10.1016/j.electacta.2013.05.052